

Statistical Process Monitoring of Isolated and Persistent Defects in Complex Geometrical Shapes

Sara Bonacina* (sara.bonacina@studenti.unipd.it)
 Daniele Zago*,[†] (daniele.zago.1@phd.unipd.it)
 Giovanna Capizzi* (capizzi@stat.unipd.it)
 Bianca Maria Colosimo[‡] (biancamaria.colosimo@polimi.it)

October 20, 2023

Abstract

Traditional Statistical Process Control methodologies face several challenges when monitoring defects in complex geometries, such as those of products obtained via Additive Manufacturing techniques. Many approaches cannot be applied in these settings due to the high dimensionality of the data and the lack of parametric and distributional assumptions on the object shapes. Motivated by a case study involving the monitoring of egg-shaped trabecular structures, we investigate two recently-proposed methodologies to detect deviations from the nominal IC model caused by excess or lack of material. Our study focuses on the detection of both isolated large changes in the geometric structure, as well as persistent small deviations. We compare the approach of Scimone et al. (2022) with Zhao and del Castillo (2021) for monitoring defects in a small Phase I sample of 3D-printed objects. While the former control chart is able to detect large defects, the latter allows the detection of nonconforming objects with persistent small defects. Furthermore, we address the fundamental issue of selecting the number of eigenvalues to be monitored in Zhao and del Castillo's method by proposing a dimensionality reduction technique based on kernel principal components. This approach is shown to provide a good detection capability even when considering a large number of eigenvalues. By leveraging the sensitivity of the two monitoring schemes to different magnitudes of nonconformities, we also propose a novel joint monitoring scheme that is capable of identifying both types of defects in the considered case study. Computer code in R and Matlab that implements these methods and replicates the results is available as part of the supplementary material.

Keywords: Additive manufacturing; Statistical process monitoring; Complex shapes; Non-parametric control charts; Phase I.

*Department of Statistics, Università degli Studi di Padova, Padua, Italy.

[†]Corresponding author.

[‡]Department of Mechanical Engineering, Politecnico di Milano, Milan, Italy.

1 Introduction

With the advancement of Industry 4.0, Additive Manufacturing (AM) technology has entered a period of rapid development, in which complex shapes can now be created beyond the limitations of traditional molding methods. Manufacturing of AM products involves the development of a computer-aided design (CAD), a digital model of the object that has to be produced by a 3D printing machine. Starting from the CAD model, the physical object is then created via a layer-by-layer deposition of material from the nozzle of the 3D printing machine. The quality of the resulting product is typically affected by several process parameters such as, among others, temperature, speed of the nozzle, and thickness of the layers (Sood et al., 2011; Garg et al., 2014; Wuest et al., 2014).

The increasing complexity of the shapes that can be produced through AM poses several challenges for inspecting and monitoring the quality of the final products. Traditional SPC methodologies can be applied to the monitoring of geometric shapes when these can be adequately represented by a set of key product characteristics (KPCs). Under this framework, summary statistics related to functional or aesthetic performance of the products are calculated from the manufactured object, and are then monitored over time using classical multivariate control chart methods to detect potential defects. However, KPCs are often ineffective at summarizing the highly complex geometries resulting from AM processes, potentially leading to suboptimal detection of defects. This is especially relevant when faults in the shape of the object do not significantly alter the KPCs under monitoring. KPC-based methodologies for complex geometric shapes were developed due to limited computational resources and specialized technology. Nowadays, the complex geometrical objects produced through AM can be measured using noncontact measurement tools, such as laser scanners, X-ray computer tomography (CT), etc. The geometry of the manufactured product can be then reconstructed based on high-dimensional noisy 3D point clouds. As the manufacturing technologies advance, appropriate SPC techniques that leverage the full geometric information of the products are required in order to complement the manufacturing process

and potentially increase the quality of the final products.

Some approaches that use geometrical information are based on surface modelling. Surface modelling is a higher-dimensional generalization of profile monitoring (see [Woodall et al., 2004](#), for a review of profile monitoring), which involves monitoring 2.5D surfaces over time using parametric or nonparametric statistical models. These models are specifically designed to monitor the surface component of objects produced through additive manufacturing processes. Parametric models for surface monitoring involve estimating the model parameters that govern the surface structure and then monitoring their stability over time. For example, one common approach is to use spatial autoregressive models ([Colosimo et al., 2008](#)) or principal component analysis ([Colosimo and Pacella, 2007](#)). Nonparametric surface models, on the other hand, aim to estimate the surface without imposing strict parametric assumptions. This approach is particularly suitable for irregular and complex surfaces since it offers greater flexibility compared to parametric methods.

The use of surface monitoring for detection of defects has been explored by several authors. For instance, [Wang et al. \(2014\)](#) define a control chart procedure after estimating the surface profile with a Gaussian-Kriging model. A further improvement on the Gaussian-Kriging approach is provided by [del Castillo et al. \(2015\)](#), who use Gaussian process modelling of the surface using a geodesic-based modelling of the covariance between points on the surface. The use of geodesic distances over Euclidean distances allows a more accurate reconstruction of the free-form surface, as well as better detection of faults. [Zhao et al. \(2022\)](#) embed a three-dimensional surface into a 2D spherical domain and apply a multi-output Gaussian process regression model to model the spherical mapping. The estimated surface is then monitored over time using standard control chart techniques.

Kernel-based surface smoothing is another approach that can be used to define control charts for monitoring surface deviations from an in-control reference model. This methodology has been developed and applied for both Phase I ([Zang and Qiu, 2018a](#)) and Phase II ([Zang and Qiu, 2018b](#)) monitoring problems. Additionally, these works address the alignment problem (registration) of surfaces reconstructed by non-contact sensor systems, which

generate unstructured data that requires pre-processing to be registered with the nominal surface.

However, these methodologies face limitations in their application to monitoring defects in objects that are produced through AM. Specifically, they typically only consider the upper surface of the objects, neglecting other potentially important characteristics of the full 3D shape of the object. Additionally, the registration and estimation phase of the surfaces can be computationally intensive, especially when considering the large point clouds obtained by noncontact measurement tools.

To address the complexity of reconstructed geometries using point clouds, other approaches for detecting shape defects compare the estimated point cloud with the nominal CAD model. This typically involves computing deviations of the manufactured product from the nominal model and creating a 3D map of these deviations, which are then monitored over time using various techniques. For instance, [Megahed et al. \(2010\)](#) and [Wells et al. \(2013\)](#) utilize quantile-quantile plots to summarize the information provided by the 3D deviation map. They then employ parametric profile monitoring schemes to identify deviations of the curve from the in-control conditions. Using this approach, only global deviations from the nominal model can be detected, as the spatial structure of the deviation map is lost in the quantile-quantile plot representation of the deviations.

[Stankus and Castillo-Villar \(2019\)](#) propose an approach based on regions of interest (ROIs) that are defined in the deviation map. Then, a generalized likelihood ratio control chart is used to monitor the average deviations within each ROI. Similarly, [Huang et al. \(2018\)](#) adopt the ROI approach and develop a statistical monitoring method that focuses on characterizing small sub-regions of complex shapes. They use synthetic indices to evaluate the nonrandom distribution of abnormal points and the plane direction deviation within a sub-region. Furthermore, [He et al. \(2017\)](#) offer a 2D version of ROI-based methods by projecting the 3D deviation map onto a plane to detect and analyze local anomalies. Although approaches based on ROIs allows for the detection of local defects, suitable definitions of ROIs are challenging for complex shapes. Moreover, the use of average deviations within a

region of interest may hinder the detection of patterned defects.

Recent methodologies have tried on addressing these issues by focusing on the free-form characteristics of the manufactured object. In their work, [Scimone et al. \(2022\)](#) propose a methodology for characterizing, modeling, and monitoring the natural variability of complex shapes. They utilize the Hausdorff distance, a metric that measures distances between shapes represented by unstructured point clouds or triangulated meshes, to identify defects in faulty products resulting from excessive or insufficient material. This is accomplished by comparing the estimated distances to a control limit, using a profile monitoring procedure. However, their approach faces potential computational challenges in the registration of the estimated point clouds with the nominal model.

In contrast, [Zhao and del Castillo \(2021\)](#) propose a different approach that avoids the need for point cloud registration. They adopt a viewpoint based on differential geometry where each shape is treated as a 2D manifold embedded in a 3D space. Within this framework, they calculate the spectrum of the Laplace-Beltrami operator of the reconstructed object, with the lower part of this spectrum providing information about the fine geometric details of the shape. This spectrum is then sequentially monitored to detect small persistent defects in the shape of the manufactured object.

The approaches of [Scimone et al. \(2022\)](#) and [Zhao and del Castillo \(2021\)](#) represent innovative approaches that can be applied to arbitrary shapes and thus can provide useful tools for improving manufacturing quality. To the best of our knowledge, no work in the literature has yet directly compared the two approaches. Furthermore, both methodologies have been evaluated in specific settings. The method of [Scimone et al. \(2022\)](#) was designed and investigated to detect large defects, thus its performance for small persistent defects remains unknown. The method of [Zhao and del Castillo \(2021\)](#) was originally discussed for online surveillance and was complemented in the early stages of the monitoring phase by a Phase I control chart.

In this work, we start from a case study involving the monitoring of egg-shaped trabecular structures, which was originally discussed in [Scimone et al. \(2022\)](#). We investigate these

two innovative methodologies in detecting deviations from the nominal IC model caused by either excess or lack of material. In our study, we focus on the detection of both isolated large changes as well as persistent small deviations to compare the performance of the two methods.

The rest of the work is structured as follows: Section 2 discusses the two considered approaches for statistical monitoring of free-form shapes. Section 3 presents the case study, detailing the trabecular egg shapes produced through AM and scanned using a non-contact sensor system. In Section 4, we discuss the application of [Scimone et al. \(2022\)](#)'s and [Zhao and del Castillo \(2021\)](#)'s method to the case study. To address the issue in determining the number of eigenvalues to monitor in [Zhao and del Castillo \(2021\)](#)'s approach, we propose supplementing their method with a dimensionality reduction approach. This allows the use of a large number of eigenvalues while retaining satisfactory performance in the detection of small shifts.

Motivated by the complementary performance of the two methods, which appear to be adept at detecting different magnitudes of defects, we further propose a joint monitoring scheme that combines the two approaches. This joint monitoring scheme is shown to be able to correctly identify all defective products in the case study. Finally, Section 5 offers some concluding remarks. R and Matlab code for implementing the control charts and reproducing the results are provided as part of the supplemental material.

2 Methodology

2.1 A Method Based on Simplicial Functional Principal Component Analysis (SFPCA)

The method presented by [Scimone et al. \(2022\)](#) belongs to the class of approaches based on deviation profile analysis. It comprises three main steps: firstly, the deviations between each product's reconstructed non-contact sensor system data and the CAD model are

computed; then, the empirical probability density function (PDF) of these deviations is estimated; finally, a profile surveillance scheme, based on a generalization of principal component analysis called simplicial functional principal component analysis (SPFCA, see [Hron et al., 2016](#)), is applied to the PDFs.

To compute the deviations from the CAD model, this methodology assumes that both the reconstructions of the products and the nominal model are represented as point clouds. The alignment of unstructured point clouds is a crucial preliminary step and is performed via the Iterative Closest Point (ICP) algorithm, which has found widespread application in image processing ([Besl and McKay, 1992](#)). This process involves solving a discrete nonlinear optimization problem: a suitable error metric is minimized by identifying the closest point in the second point cloud for each point in the first point cloud. The original ICP algorithm has a computational cost of $O(N_1 \cdot N_2)$, where N_1 and N_2 are the number of points in the two point clouds to align. Due to the large amount of points in point clouds obtained by noncontact measurement tools, the computational cost of the standard ICP algorithm is typically prohibitive in practice. To address this limitation, recent versions, including the one utilized by [Scimone et al. \(2022\)](#), perform registration by selecting a subset of points known as reference points. The resulting pairs of reference points are then used to estimate the rotation and translation matrices of the rigid transformation that aligns the point clouds. The selection of reference points is a critical issue in the methodology, since different choices can lead to different alignments for the same pair of point clouds. Additionally, the iterative and non-convex nature of the ICP algorithm means that it may converge to a suboptimal solution instead of a global optimum.

After alignment of the point clouds, a suitable distance between the point cloud of each product and the point cloud of the nominal model is considered. Specifically, let S_j for $j = 1, \dots, N$ represent the point cloud $\{p_1^j, \dots, p_{M_j}^j\}$ consisting of M_j points for the j -th product. Furthermore, let $P = \{p_1^p, \dots, p_{M_p}^p\}$ be the point cloud of M_p points for the CAD model. The Hausdorff distance ([Hausdorff, 1914](#)) between point clouds S_j and P is defined

as

$$d_H(S_j, P) := \max \left\{ \sup_{s \in S_j} \inf_{p \in P} d(s, p), \sup_{p \in P} \inf_{s \in S_j} d(s, p) \right\}. \quad (1)$$

The Hausdorff distance is a global measure of deviation from the nominal model. Furthermore, from its definition two deviation maps can be identified,

$$d_{S_j} : P \rightarrow C_j, \quad d_{S_j}(p) := \inf_{s \in S_j} d(s, p), \quad (2)$$

and

$$d_P^j : S_j \rightarrow K_j, \quad d_P^j(s) := \inf_{p \in P} d(s, p), \quad (3)$$

where K_j and C_j are intervals in \mathbb{R} . d_{S_j} and d_P^j represent the distance of each point in P from S_j and the distance of each point in S_j from P respectively. Note that, in general, $\sup_{s \in S_j} d_P^j(s) \neq \sup_{p \in P} d_{S_j}(p)$, as S_j and P may have different domains.

For instance, if S_j has more points than P , the distances calculated from the d_P^j map would be high because S_j contains points that do not belong to P . This situation can occur when there are defects in the produced piece due to excess material. If instead S_j has fewer points than P , the distances calculated from the d_{S_j} map would again be high because P contains points that do not belong to S_j . This situation occurs in the case of defects due to missing material. In [Scimone et al. \(2022\)](#), these observations are exploited to construct a bidirectional interpretable monitoring scheme to detect object defects. The deviation maps, d_P^j and d_{S_j} , yield two high-dimensional deviation vectors, D_P^j and D_{S_j} , for each point cloud S_j . To summarize this information, the authors follow the approach of [Menafoglio et al. \(2018\)](#) and synthesize the deviation vectors using their empirical PDFs. The authors use Bernstein polynomial estimator ([Vitale, 1975](#); [Leblanc, 2010](#)) to obtain two sets of PDFs, $\mathbf{f}_S := \{\hat{f}_{S_j}, j = 1, \dots, N\}$ and $\mathbf{f}_P := \{\hat{f}_P^j, j = 1, \dots, N\}$, which capture the bidirectional nature of the deviation maps d_{S_j} and d_P^j .

In order to monitor process stability and detect any out-of-control sections, SFPCA is employed separately for the data sets \mathbf{f}_S and \mathbf{f}_P . SFPCA is a dimensionality reduction

technique that can be applied to sets of probability density functions, and results in a vector of principal component scores associated to each element of \mathbf{f}_S and \mathbf{f}_P (Hron et al., 2016). Refer to Appendix A for an introduction on SFPCA. In PCA-based surveillance approaches, two control statistics are defined: the Hotelling T^2 statistic is used to identify anomalies in the PDFs based on the scores along the principal components, while the Q statistic is used to identify anomalies in the residual component. The expressions of the monitoring statistics for the \mathbf{f}_s and \mathbf{f}_P data sets, $(T^{2(S)}, Q^{(S)})$ and $(T^{2(P)}, Q^{(P)})$ respectively, as well as their control limits, are given in Appendix A.1. The four control charts are applied simultaneously in a combined monitoring scheme, signalling and alarm whenever any of them detects an out-of-control situation. Leveraging the previous observations on the role of the two deviation maps in Equations (2) and (3), the pair of statistics $(T^{2(P)}, Q^{(P)})$ is expected to indicate excess material compared to the CAD model, while the pair $(T^{2(S)}, Q^{(S)})$ should indicate defects due to a lack of material. This provides a useful tool for post-diagnostic analysis, as the charts can both identify out-of-control samples as well as indicating the type of defect.

This methodology is adaptable to complex geometries and can be applied to point cloud data without point-to-point correspondence or defined ROIs. Furthermore, it does not rely on any distributional assumptions such as normality of the deviations, making it a generalization of previous methods such as the one introduced by Wells et al. (2013). However, the preliminary registration phase presents substantial challenges, including a high computational cost and potential varying solutions obtained by the modified ICP algorithm.

2.2 A Method Based on the Spectrum of the Laplace-Beltrami Operator (LB)

The monitoring procedure proposed by Zhao and del Castillo (2021) is an innovative contribution in manifold surveillance which takes a completely different perspective compared to previous methodologies. Due to its unique approach, the reconstructed point clouds do

not need to have the same number of points. Furthermore, point cloud or mesh registration is avoided.

Their methodology involves two main steps: first, tools from differential geometry are used to extract information about the object’s structure, which is then represented by eigenvalues of the Laplace-Beltrami (LB) operator (Kreyszig, 1991); then, these these eigenvalues are monitored using a non-parametric multivariate control chart. Differential geometry studies properties of curves, surfaces, and higher-dimensional geometrical objects using tools from calculus and linear algebra. The aim is to deduce properties that govern the entire structure of the object under analysis by starting from local properties and terminology that characterize the neighborhood of a point on a surface. See Appendix A.2 for a review of basic concepts and terminology of differential geometry. The monitoring procedure of Zhao and del Castillo (2021) relies on the manifold hypothesis, namely the assumption the data in an n -dimensional curved space (the “ambient space”) actually lie in a lower-dimensional space k (the “intrinsic dimension” of the manifold). Any property of a manifold \mathcal{M} that can be computed without resorting to the coordinates of the ambient space, but only using the intrinsic coordinates x^1, \dots, x^k of the manifold, is called an “intrinsic property” of the manifold. Furthermore, any geometric property of a manifold that remains unchanged after the application of a given transformation is called “invariant” with respect to that transformation. The intrinsic properties of a manifold in a Euclidean space, on which the methodology proposed by Zhao and del Castillo (2021) is based, are invariant with respect to rigid transformations. This key property allows their proposed monitoring procedure to avoid the preliminary registration phase of point clouds or meshes.

The methodology described below is developed for data in mesh format, but it can also be extended to data represented as point clouds or voxels (Zhao, 2022). The LB operator $\Delta_{\mathcal{M}}f$ of a function f associated to a manifold \mathcal{M} (Appendix A.2.2) can be summarized by its spectrum, which consists of the eigenvalues $\{\lambda_i\}_{i=0}^{\infty}$, that are solutions of the eigenvalue problem

$$\Delta_{\mathcal{M}}f = \lambda f, \tag{4}$$

The spectrum of the LB operator is increasing and non-negative (Chavel et al., 1984) and has been found to better summarize the geometric and topological properties of the manifold than other measures such as surface area (Reuter et al., 2009).

Using the eigenvalue decomposition of the matrix L^t defined in Equation (A.13), the spectrum $\{\lambda_i\}_{i=0}^{\infty}$ can be approximated using the discrete LB operator obtained using a mesh representation of the manifold. The calculation of the approximate spectrum is numerically stable unless the object presents exact symmetries, which are rarely observed in scanned objects (Patanè, 2017; Zhao and del Castillo, 2021). Furthermore, it has been shown that only the lower part of the spectrum is needed for detecting defects and it is robust to moderate amounts of noise (Zhao and del Castillo, 2021). Calculation of the first K eigenvalues can be performed using for instance the Arnoldi algorithm (Arnoldi, 1951) implemented in the `eigs` function in Matlab. The computational cost associated with the calculation of the first K eigenvalues is $O(K \cdot m)$, which is reasonable even for large m .

2.2.1 Nonparametric Phase I Control Chart

After the lower part of the spectrum $\lambda_1, \lambda_2, \dots, \lambda_K$ of the discrete LB operator is obtained for each manufactured product, the eigenvalues are then monitored using a nonparametric procedure since their distribution is non-normal (Zhao and del Castillo, 2021). In order to do so as new objects are being sequentially observed (Phase II), the authors use a modified version of the self-starting control chart proposed by Chen et al. (2016). Self-starting charts do not typically require a large pre-sampling observation set, but may have difficulty detecting out-of-control observations in the initial stages of surveillance (Qiu, 2013). To complement this control chart, the self-starting control chart is complemented by a permutation-based nonparametric retrospective (Phase I) control chart (Capizzi and Masarotto, 2017) during the early stages of sequential monitoring. For a discussion on the difference between Phase I and Phase II process monitoring, refer for example to Qiu (2013).

For the purpose of this paper and, particularly, of the case study described in Sec-

tion 3, the monitoring procedure of Zhao and del Castillo (2021) will be considered in a completely-offline Phase I setting. Therefore, only the permutation-based Phase I control chart, henceforth referred to as the `mphase1` control chart, will be considered in the following discussion. Here, we will provide a concise summary of the steps involved in applying the `mphase1` procedure to the eigenvalues of the LB operator for Phase I analysis of complex manifold data. Let λ_{ji} be the i -th ordered eigenvalue, $i = 1, \dots, K$, associated with the j -th manufactured piece, $j = 1, \dots, N$, with $K < N$. The multivariate signed ranks (Oja, 2010) are calculated on the standardized eigenvalues, resulting in K -dimensional vectors \mathbf{u}_j . This transformation reflects both the direction and the magnitude of the distance of an observation from the center of the data. A linear regression model is then fitted to the signed ranks,

$$\mathbf{u}_j = \boldsymbol{\beta} + \sum_{\tau=2}^{N-1} \boldsymbol{\beta}_{\text{step},\tau} \cdot I(j \geq \tau) + \varepsilon_j, \quad j = 1, \dots, N, \quad (5)$$

where $\boldsymbol{\beta}$ and $\{\boldsymbol{\beta}_{\text{step},\tau}\}_{\tau=2}^{N-1}$ are unknown K -dimensional parameters, $I(\cdot)$ is the indicator function, and ε_j is an error term. Here, $\boldsymbol{\beta}$ represents the average level of the signed ranks, while each $\boldsymbol{\beta}_{\text{step},\tau}$ introduces a level change starting from time τ and involving all subsequent observations. Note that (5) is a simplified version of the original linear model proposed in Capizzi and Masarotto (2017) that does not consider isolated shifts. When data not comprised of rational subgroups but rather individual observations, discriminating isolated shifts from outlying observations due to heavy-tailed in-control distributions using a distribution-free control chart is impossible (see Section 3.1 of Capizzi and Masarotto, 2017).

Using a forward stepwise search algorithm, $H < N - 1$ parameters associated with the most plausible change points are selected. An overall p -value is then calculated to test the global stability of the process by aggregating H elementary statistics and using a permutation-based approach (Pesarin, 2001). When an alarm is triggered, the adaptive LASSO algorithm (Zou, 2006) is then used as a diagnostic tool to identify the eigenvalues that led to the out-of-control condition.

3 A Case Study

The case study considered in this paper was first described by [Scimone et al. \(2022\)](#). Each manufactured product is characterized by an egg-shaped trabecular structure, and will be referred to simply as “egg” in the rest of the paper. The trabecular structure of the egg consists of “struts” and “nodes”, where struts are structural components arranged along the edges of polygons, and nodes are the points where two or more struts meet. Refer to [Scimone et al. \(2022\)](#) for an in-depth discussion of the structural characteristic of the eggs.

Each egg was produced using Fused Deposition Modeling (FDM), a special AM process which involves heating thermoplastic material, extruding it through a nozzle, and depositing it on a platform layer by layer to construct the objects. X-ray CT was then used to scan and digitally reconstruct the final product. X-ray CT measurements produce voxel-based reconstructions that can be represented as grayscale images, where the pixel intensity indicates the measured density of the material. The reconstructed surface is then converted to a mesh format and saved in the Standard Triangulation Language (STL) format which is commonly used in CAD software.

During the egg production process, it is common to encounter geometric defects due to the complexity of the manufacturing process. This analysis focuses on nonconformities that are representative of the most common anomalies in FDM and AM processes: local geometric distortions, pores, and cracks. In general, geometric errors can be attributed to either an excess or lack of material, which can be caused by various factors. Excess material, known as the “stringing effect”, occurs when thin and unsightly plastic threads form in different parts of the object. This happens when the molten filament inside the printer nozzle escapes and solidifies, creating threads attached to the printed parts. The stringing effect is generally a result of a suboptimal choice of process parameters, such as speed of the printer and nozzle temperature. Local irregularities in the struts of a nonconforming egg due to excess material, a condition which could affect both the quality and the structural integrity of the final product. On the other hand, the absence of material

(e.g. by missing a strut) can be attributed to issues such as a lack of local adhesion between layers, interrupted material flow, or a misaligned nozzle.

The present case study involves 13 eggs scanned using X-ray CT and represented by point clouds of approximately 15 000 points, with some slight variations across the objects. Of the 13 manufactured objects, the first 8 are conforming to the nominal model and are considered in-control, while the remaining 5 are characterized by nonconformities and are deemed out-of-control. The first out-of-control egg (the ninth egg) has been deliberately designed by removing one of the struts from a 3D-printed egg. The remaining four eggs display anomalies of varying intensities due to the use of different pigments in the thermoplastic material compared to the IC eggs. The abnormal behavior of the polymer filament, due to the different pigmentation, affects the heating and extrusion process, ultimately resulting in excess material being deposited around the struts. The objective of this work is to compare the control chart procedures described in Section 2 to detect the abnormalities in the defective products.

Compared to the methodologies in Section 2, the other approaches discussed in Section 1 are not applicable to the present case study. Methods based on surface surveillance cannot be applied to detect the defective objects because the eggs have three-dimensional free-form geometries. These shapes cannot be adequately described with regular parametric or nonparametric 2.5D surface models. Additionally, the high dimensionality of point clouds makes the surface registration step (Zang and Qiu, 2018a,b) computationally intractable. Furthermore, the analysis is complicated by the fact that i) no distributional assumptions are placed on the point cloud measurements, ii) the number of points obtained from X-Ray CT scanning varies between point clouds, and iii) defining ROIs for the case study is challenging due to the complex geometric structure. Therefore, the approaches of Wells et al. (2013), He et al. (2017), and Stankus and Castillo-Villar (2019) cannot be applied. On the other hand, the methodologies presented in Section 2.1 and Section 2.2 provide two competing strategies for the surveillance of complex geometries, which overcome the limitations of the previous approaches.

Note that this work will be focused on the comparison of these two methodologies in a Phase I scenario with a low number of samples. For short-run productions, such as the present case study, it is not feasible to adopt an online surveillance approach due to the limited number of available samples. Furthermore, in this paper the performance of the methodologies proposed by [Scimone et al. \(2022\)](#) and [Zhao and del Castillo \(2021\)](#) is evaluated under different conditions than those considered by the authors. In their work, [Scimone et al. \(2022\)](#) specifically designed their methodology for monitoring eggs that are similar to those discussed in this section. However, their application was evaluated by considering only isolated and highly pronounced defects, whereas this case study also examines persistent defects. Conversely, the control chart developed by [Zhao and del Castillo \(2021\)](#) was primarily intended for online surveillance of small persistent defects, with the nonparametric control chart described in Section 2.2.1 serving as a complementary tool during the early stages of monitoring. Instead, this paper analyzes and discusses its application in a fully-retrospective Phase I context.

4 Application of the Surveillance Schemes to Monitor Egg Defects

In this section, we will apply the monitoring procedures discussed in Section 2 to the dataset from our case study and compare their ability to detect the various defects described in Section 3. Additionally, we discuss the issue of selecting the number of eigenvalues of the LB operator for monitoring defects using [Zhao and del Castillo \(2021\)](#)'s approach for low sample sizes. Currently, there are limited theoretical and practical guidelines to guide this selection, especially for complex-shaped objects like the eggs in our case study. Motivated by the issue, we propose a generalization of the approach presented by ([Zhao and del Castillo, 2021](#)) that uses a dimensionality reduction approach to guide the selection of eigenvalues. The proposed approach is shown to adequately detect detect the persistent small defects due to excess material. Furthermore, we compare the two methodologies and

further propose a joint monitoring scheme that appears to combine the strengths of the two approaches. This joint monitoring scheme can be implemented using a simple FAP correction (Bonferroni, 1936) and is shown to provide satisfactory detection capabilities for both types of defects. The analyses were performed using R and Matlab, and code that reproduces the results can be found in the supplemental material.

4.1 Surveillance of Deviation Profiles Using SFPCA

We first consider sequential detection of faulty products using the SFPCA-based monitoring procedure discussed in Section 2.1. The deviation vectors, D_P^j and D_{S_j} , are calculated for each object from the registered point cloud. The deviations are then transformed on a logarithmic scale to account for the large number of elements close to or equal to zero, as well as to reduce the asymmetry in their distribution. Next, the PDFs of the deviation vectors $\log D_P^j$ and $\log D_{S_j}$ are obtained and the simplicial functional principal components of the PDFs are estimated according to the procedure detailed in Appendix A. We retain only the first estimated principal component, since it is already enough to explain 98% of the total variability in the density of the deviation vectors. This threshold value is consistent with the recommendations given by Menafoglio et al. (2018). Control statistics (T^2 and Q) and their respective control limits, $UCL_\alpha(T^2)$ and $UCL_\alpha(Q)$, are then calculated as described by Equations (A.5)–(A.8), with an overall FAP of $\alpha^* = 0.05$.

The control charts $T^{2(P)}$ and $Q^{(P)}$ are depicted in Figure 1, with the black lines representing the respective control limits. From the discussion in Section 2.1, this pair of control charts aims to identify observations that exhibit nonconformities due to excess material. Notice that the neither of the two charts signals an alarm for the last four objects, which are characterized by small defects. Each statistic T_j^2 is constructed with information related to a specific observation, making it a Shewhart-type chart. In the SPC literature, it is a well-known fact that Shewhart-type charts are generally not capable of detecting persistent and small-intensity changes (Qiu, 2013), which are precisely the types of excess material defects being considered in this case study.

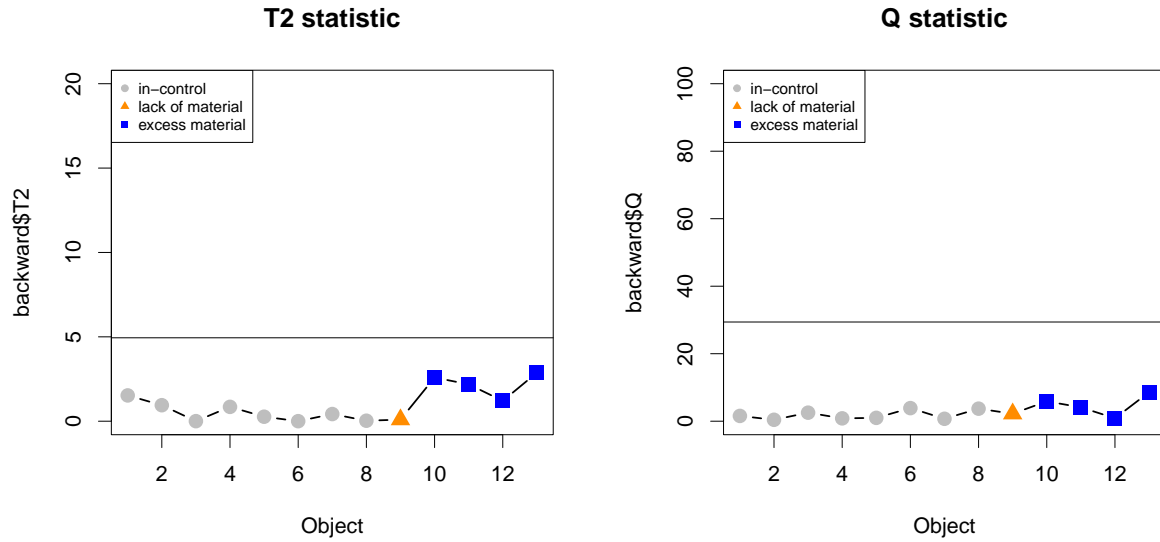


Figure 1: Control charts for the density functions \hat{f}_P^j using one principal component. The solid black line indicates the upper control limit of each control chart.

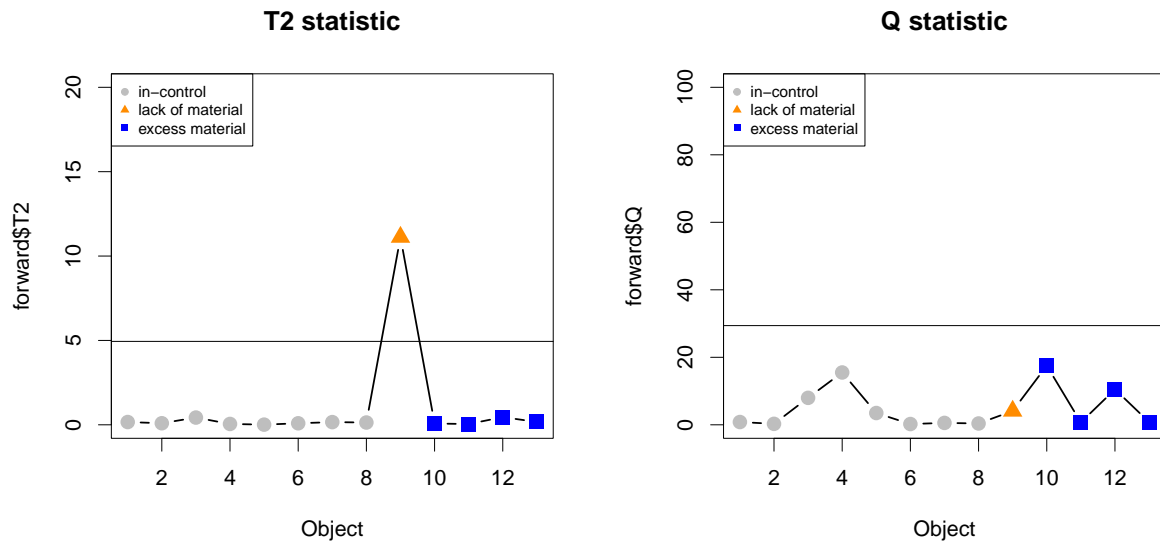


Figure 2: Control charts for the density functions \hat{f}_{S_j} using one principal component. The solid black line indicates the upper control limit of each control chart.

Figure 2 shows the control charts for monitoring the density functions \hat{f}_{S_j} and the associated control limits. Recall that these PDFs summarize the information regarding the distances of the points of the nominal model from those of the j -th egg (Section 2.1). Consequently, the corresponding control charts are designed to identify anomalous observations characterized by a lack of material. In this scenario, the control chart correctly triggers an alarm for the ninth egg, which is missing a strut. This defect is both isolated and large in magnitude, and can be effectively captured by the Shewhart-type T^2 statistic using the first principal component of \hat{f}_{S_j} .

We conclude that the SFPCA-based procedure can be a useful tool for detecting large, isolated defects due to its Shewhart-type nature. However, its shortcomings are displayed when considering smaller sustained shifts, which appear to be substantially harder to detect using this methodology.

4.2 Surveillance of the Spectrum of the Discrete LB Operator

Here, we detail the application of the methodology discussed in Section 2.2 to our case study. Once the discrete LB operator has been calculated on the mesh of each egg, the lower part of the spectrum is computed using the L_{sym} matrix in Equation (A.15). Next, the nonparametric control chart described in Section 2.2.1 is applied to the lower-part of the spectrum, after selecting a suitable number K of eigenvalues to monitor. It is important to note that the number of eigenvalues considered should be smaller than the number of available observations. Currently, however, there is no clear-cut criteria to determine the number of eigenvalues of the LB operator to be used for defect detection. Given the small sample size of 13 products, we consider the performance of the control chart when monitoring 2 to 5 eigenvalues. As mentioned by (Zhao and del Castillo, 2021), due to numerical approximation errors, the first eigenvalues may have very small negative values, and should not be considered in the analysis. In our analysis, we remove the first 15 eigenvalues since they are mostly on the order of 10^{-22} . The performance of the `mphase1` control chart is also evaluated when varying the minimum length of a persistent change, if

Table 1: Results of the monitoring of the LB spectrum of the 13 objects for various values of the number of monitored eigenvalues (K) and minimum length of the persistent change (l_{\min}). The location (object) of the detected sustained change and the p -value of the global process stability test are indicated. The FAP is set to 0.05 and the symbol ‘-’ indicates that no change was detected by the procedure.

K	l_{\min}	Change location (object)	p -value
2	2	10	0.016
	3	–	0.076
	4	–	0.955
3	2	10	0.015
	3	9	0.045
	4	–	0.425
4	2	10	0.008
	3	9	0.028
	4	–	0.112
5	2	4 and 10	0.006
	3	4 and 9	0.025
	4	–	0.107

present. Given the small sample size, it seems reasonable to assume the presence of even very short changes. Therefore, we consider a minimum length of 2, 3, or 4 for the step change in the nonparametric control chart.

Table 1 presents the results of the surveillance of the 13 objects based on the number of eigenvalues considered and the minimum length of the persistent change, with a FAP of $\alpha = 0.05$. The estimated change point(s) and the p -value related to the global process stability test are also indicated. The results suggest that $K = 2, 3, \text{ or } 4$ eigenvalues are sufficient to correctly identify all out-of-control objects characterized by an excess of material (from the tenth to the thirteenth object) Furthermore, for minimum shift lengths larger than 3, the control chart is not able to detect any significant changes. Therefore, we conclude that a minimum shift length of 2 or 3 is appropriate for detecting the OC objects in the present case study.

When $K = 5$ eigenvalues are used in the monitoring, the chart erroneously raises an alarm for the fourth object, which is actually in-control. This finding aligns with the results of [Zhao and del Castillo \(2021\)](#), who showed through simulation studies that considering a

large number of eigenvalues is counterproductive for the chart’s performance. According to their results, this is due to the fact that only the lower part of the spectrum of the discrete LB operator contains relevant information about the geometric properties of the product, while higher eigenvalues also contain some “noise” (Reuter et al., 2009). The object without a strut (the ninth) can only be identified when considering $K = 3$ or 4 eigenvalues with a minimum change length $l_{\min} = 3$. Identification of this change using this methodology is significantly more challenging because it is a large localized defect. Recalling the discussion in Section 2.2.1, detecting large changes with individual observations using a distribution-free control chart poses significant challenges.

Figure 3 shows the post-signal diagnostic plot for the nonparametric control chart which monitor $K = 4$ eigenvalues with minimum step change length $l_{\min} = 3$. From the plots, we can observe that the sustained change is detected in the 17th eigenvalue starting from the 9th observation.

As is customary during Phase I analysis, any observations identified as out-of-control are removed once an alarm is raised, and the procedure is repeated. Once the OC observations are removed, a second application of the `mphase1` control chart correctly results in the process being declared as in-control.

4.2.1 Addressing the Selection of the Number of Eigenvalues

The Phase I nonparametric control chart using Zhao and del Castillo (2021)’s approach requires the uneasy choice of selecting the number of eigenvalues of the LB operator to monitor. In the case of complex shapes, adjacent LB eigenvalues can be highly correlated, indicating that they may be representing similar shape information (as can be seen in Figure 3). Additionally, the number of LB eigenvalues to monitor must be smaller than the number of observed data points in order to apply the `mphase1` control chart.

To address these limitations, we propose summarizing the information contained by the LB spectrum by applying dimensionality reduction techniques. Specifically, we consider from the 15th to the 100th eigenvalue of the LB operator and apply the `mphase1` control

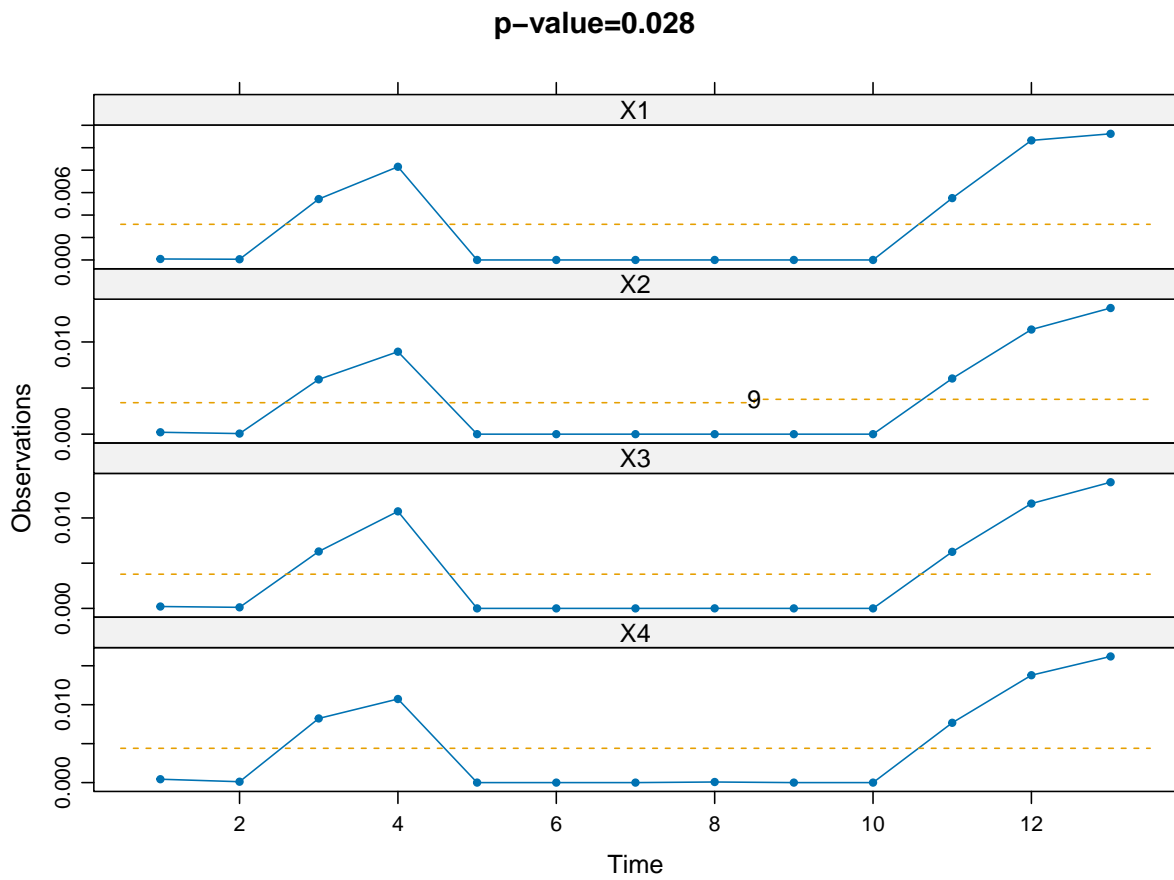


Figure 3: Post-diagnostic analysis of the `mphase1` procedure, using $K = 4$ eigenvalues and minimum length of step change $l_{\min} = 3$. The dashed line in the second plot shows the detected sustained change in the 17th eigenvalue of the LB operator, starting from the 9th observation.

Table 2: Results of the monitoring of the LB spectrum of the 13 objects on the first two directions obtained by the PCA and kPCA methods, termed LB-PCA and LB-kPCA, respectively. The minimum length of the persistent change is set to 2. The starting time (object) of the change, which affects all subsequent observations until the end of the process or until another change is identified, the p -value related to the global process stability test, and the post-diagnostic p -value obtained by repeating the procedure after removing the objects identified as OC are indicated. The best performance is highlighted in bold.

Method	Change location (object)	p -value	Post-diagnostic p -value
LB-PCA	10	0.011	0.029
LB-kPCA	10	0.004	0.084

chart to a) the first two principal components (Mardia et al., 1979) of the eigenvalues, which explain 96% of the total variability, and b) the first two kernel principal components of the eigenvalues obtained using radial basis function (Schölkopf et al., 1998). The calculation of kernel principal components was performed using the R package kernlab (Karatzoglou et al., 2004, 2023). Due to the low sample size, we set the minimum length for a step change in the `mphase1` procedure to 2.

The results presented in Table 2 demonstrate the effectiveness of applying the `mphase1` chart in detecting the change location after applying dimensionality reduction. It can be seen that that the `mphase1` control chart applied to the first two principal components obtained through either standard PCA or kPCA correctly identify a sustained change starting from the tenth object. However, when the OC observations are removed from the sample, a second application of the `mphase1` chart PCA again detects a change in the first two principal components. This OC signal is considered to be spurious, since the change is identified from the 5th object onwards. On the other hand, a second application of the `mphase1` chart using kPCA does not detect any significant shape defect after removing the OC observations.

In conclusion, it appears that monitoring the spectrum of the LB operator can be an effective approach for detecting small and persistent changes in the shape of the manufactured products. However, due to the inherent limitations of the control chart procedure, detection of large isolated shifts seems to pose a significant challenge.

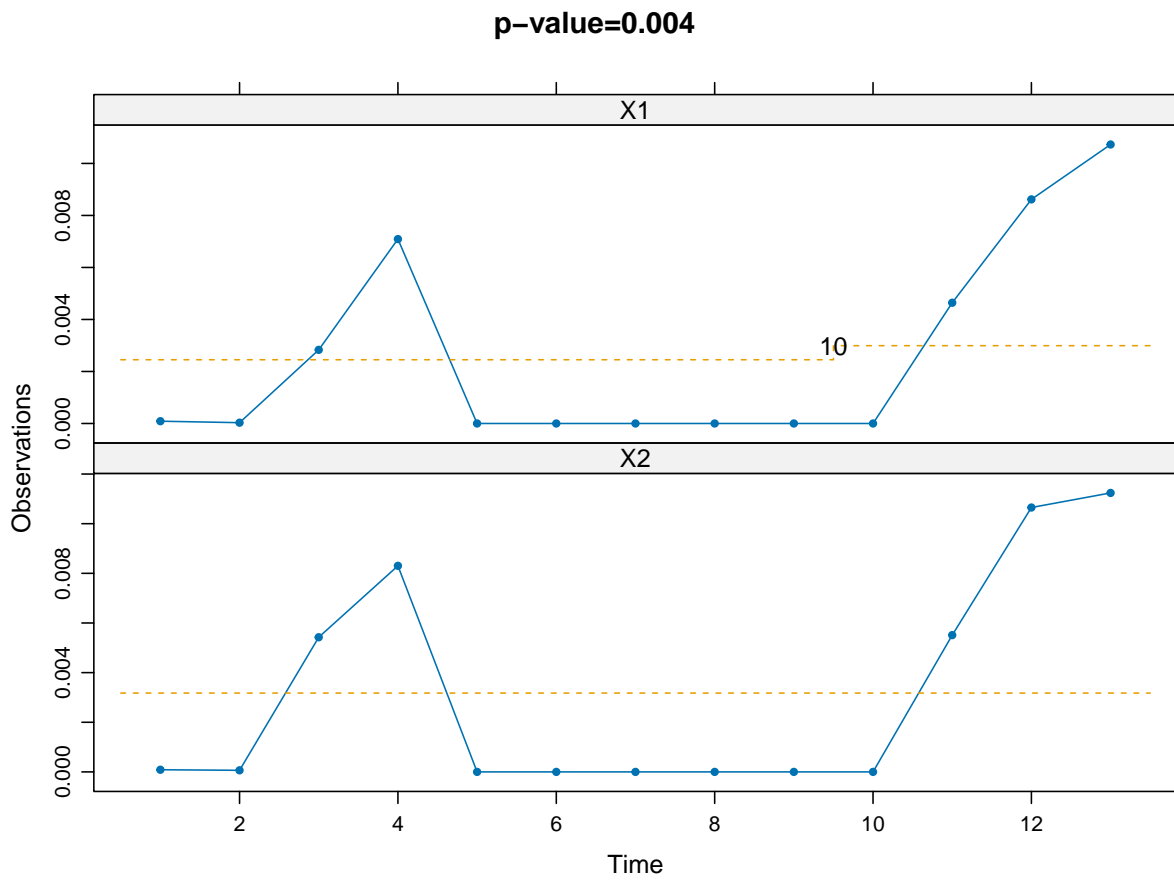


Figure 4: Post-diagnostic analysis of the `mphase1` procedure on the first two kernel principal components obtained by the `kPCA` procedure applied to LB eigenvalues 15 to 100. The minimum length of change is equal to 2. The dashed line in the second plot shows the detected sustained change in the first kernel principal component.

4.3 Joint Surveillance of Isolated and Persistent Defects

The results presented in Sections 4.1 and 4.2 indicate that the SFPCA- and LB-based methodologies can be used to detect different types of defects in complex shapes. The monitoring procedure proposed by [Scimone et al. \(2022\)](#) effectively detects isolated large defects, but it is not sensitive to small changes. On the other hand, a Phase I control chart using the approach of [Zhao and del Castillo \(2021\)](#) is adept at detecting small persistent changes but struggles to identify isolated large defects. It thus appears natural to take advantage of the complementary nature of the two methods to combine them into a joint monitoring scheme, which can possibly be useful to detect both isolated and persistent defects. By simultaneously implementing the two approaches and adjusting the joint FAP using the Bonferroni correction ([Bonferroni, 1936](#)), the combined methodology should take advantage of the strengths of both methods and deliver satisfactory performance for detecting both isolated and persistent changes.

The results obtained from the joint monitoring scheme, with an overall FAP of 0.05, are summarized in Table 3. In the joint monitoring scheme, the `mphase1` control chart is applied to the first two kernel principal components derived from the kPCA algorithm as described in Section 4.2.1. The results show that the combined methodology successfully detects all defects present in the sample. Furthermore, by inspecting the post-diagnostic plots associated to each monitoring procedure (Figures 1, 2 and 4, with different control limits and p -values), the nature of the defects detected by each control chart can be easily deduced.

4.3.1 Post-Diagnostic Analysis of the Defects

After a change has been detected, defects on the OC products can be visualized using the ICP algorithm to align the detected out-of-control shape with the nominal model ([Zhao and del Castillo, 2021](#)). This allows inspection of the exact locations in which the manufactured product displays substantial deviations from the CAD model. In the context of post-diagnostic analysis, the use of the ICP algorithm is computationally feasible since it is

Table 3: Results of the joint monitoring scheme using the SFPCA- and LB-based approaches with an overall FAP of 0.05. The LB-based approach (LB-kPCA) is applied to the first two directions obtained by the kPCA method, with a minimum length of the persistent change set to 2. The location of the detected defects, as well as the type of shift, is indicated.

Method	FAP	Change location (object)	Shift type
SFPCA	0.025	9	Isolated
LB-kPCA	0.025	10	Persistent
Joint scheme	0.05	9 and 10	Isolated and persistent

only applied to the subset products identified as nonconforming. Figure 5 illustrates the detected nonconformities obtained after performing post-diagnostic analysis on the tenth egg with the ICP algorithm. The colors displayed on the egg indicate the extent of variation between the manufactured piece and the CAD model, simplifying the visual identification of the defects.

5 Conclusions

In this work, we compare two recently-proposed control chart for statistical process monitoring of complex shapes, resulting from additive manufacturing processes. We consider a case study previously discussed by [Scimone et al. \(2022\)](#), where a small sample of egg-shaped trabecular structures is monitored to detect deviations from the nominal IC model caused by excess or lack of material. The present work considers a different scenario than the one presented in their paper, which considers large isolated shape changes, because we also focus on the detection of small, persistent defects. After reviewing classical approaches for statistical shape monitoring, we discuss the challenges of applying these methodologies to complex 3D objects obtained via AM.

We then compare the control chart of [Scimone et al. \(2022\)](#) with a methodology based on the proposal of [Zhao and del Castillo \(2021\)](#) in monitoring defects in a retrospective, Phase I setting ([Qiu, 2013](#)). This is a different approach than the one considered by [Zhao and del Castillo \(2021\)](#), as the authors focus on online detection (Phase II).

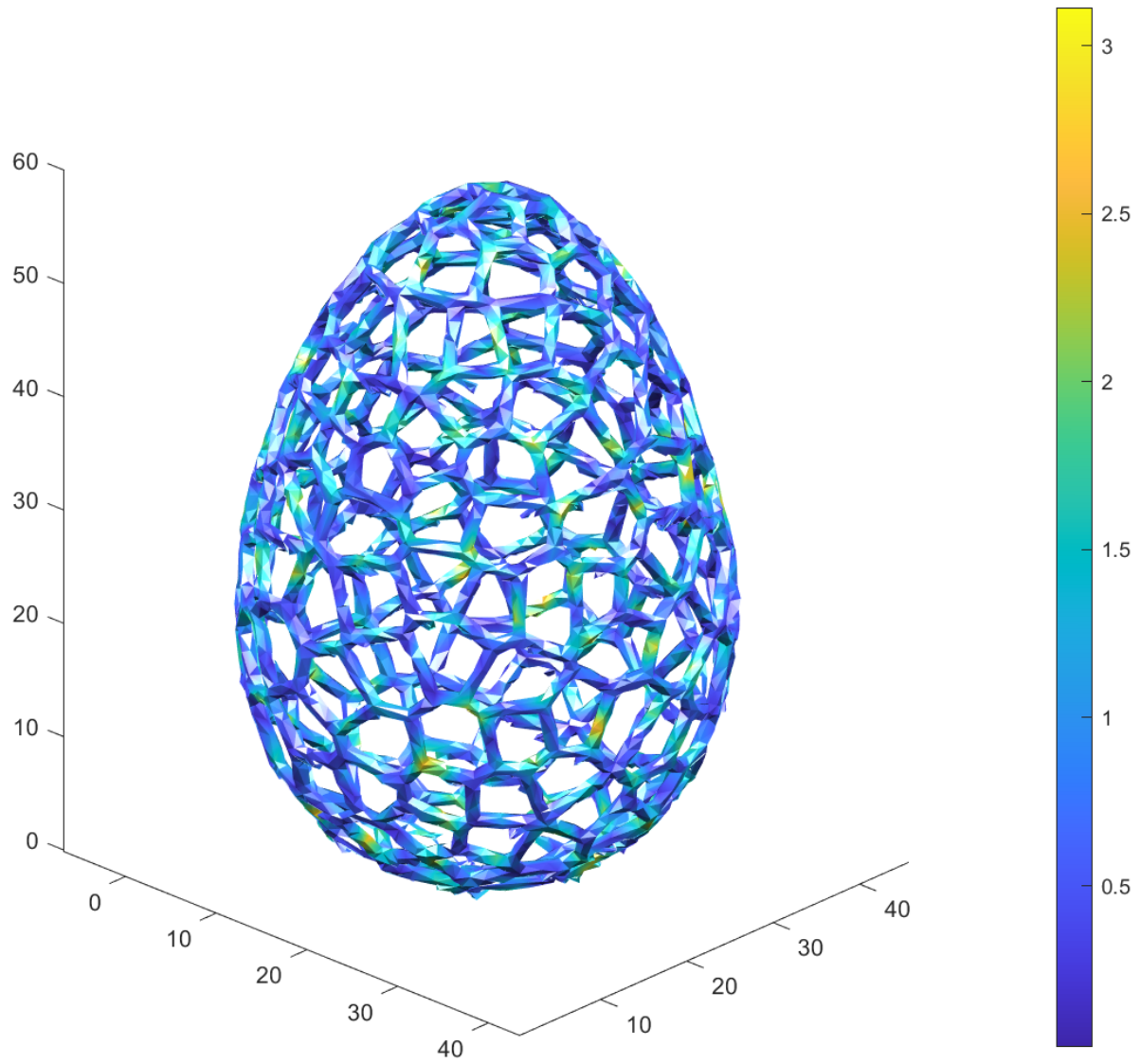


Figure 5: Post-diagnostic analysis of the tenth egg obtained with the ICP algorithm. The yellow areas indicate an excess of material in the manufactured object compared to the nominal CAD model, while the blue areas indicate the absence of discrepancies.

The results show that the two approaches complement each other in detecting nonconforming objects. While the control chart of [Scimone et al. \(2022\)](#) is able to identify large, isolated changes in the shape of the object, [Zhao and del Castillo \(2021\)](#)'s approach is conversely able to detect persistent small defects. Furthermore, we find consistent results with the latter's simulation study, which shows that increasing the number of eigenvalues of the Laplace-Beltrami operator to be monitored has a negative impact on the performance of the control chart. Furthermore, to address the issue of selecting the exact number of eigenvalues to monitor, we propose to apply a dimensionality reduction technique on the estimated eigenvalues prior to the application of the control chart. This preprocessing step appears to mitigate the problem of choosing the number of eigenvalues, while still being able to identify nonconforming objects due to the small persistent shift.

Finally, by leveraging the different sensitivity of the two monitoring schemes to isolated and persistent type of defects, we propose to apply the two approaches in a single, joint monitoring scheme. By combining the strengths of each method, we show that our proposed joint monitoring scheme is capable of identifying both types of defects in the considered case study.

As a final remark, we note that the idea of combining the spectral decomposition of the Laplace-Beltrami operator with dimensionality reduction can be further studied for monitoring other types of structured data under in low sample size scenarios. For instance, one could apply a similar idea to sequentially monitor changes in network-type data by applying dimensionality reduction on the spectral decomposition of the Laplacian matrix associated to the networks ([Chung, 1996](#)). This is left as a topic for future research.

Data availability statement

The authors confirm that the data supporting the findings of this study are available within the article and its supplementary materials.

Competing interests statement

The authors have no relevant financial or non-financial interests to disclose.

References

- Aitchison, J. (2003), *The Statistical Analysis of Compositional Data*, Caldwell, NJ: Blackburn Press.
- Arnoldi, W. E. (1951), “The Principle of Minimized Iterations in the Solution of the Matrix Eigenvalue Problem,” *Quarterly of Applied Mathematics*, 9, 17–29.
- Besl, P. and McKay, N. D. (1992), “A Method for Registration of 3-D Shapes,” *IEEE Transactions on Pattern Analysis and Machine Intelligence*, 14, 239–256.
- Bonferroni, C. E. (1936), *Teoria statistica delle classi e calcolo delle probabilità*, Seeber.
- Capizzi, G. and Masarotto, G. (2017), “Phase I Distribution-Free Analysis of Multivariate Data,” *Technometrics*, 59, 484–495.
- Chavel, I., Randol, B., and Dodziuk, J. (1984), *Eigenvalues in Riemannian Geometry*, Orlando: Academic Press.
- Chen, N., Zi, X., and Zou, C. (2016), “A Distribution-Free Multivariate Control Chart,” *Technometrics*, 58, 448–459.
- Chung, F. R. K. (1996), *Spectral Graph Theory*, Providence, R.I: American Mathematical Society.
- Colosimo, B. M. and Pacella, M. (2007), “On the Use of Principal Component Analysis to Identify Systematic Patterns in Roundness Profiles,” *Quality and Reliability Engineering International*, 23, 707–725.

- Colosimo, B. M., Semeraro, Q., and Pacella, M. (2008), “Statistical Process Control for Geometric Specifications: On the Monitoring of Roundness Profiles,” *Journal of Quality Technology*, 40, 1–18.
- del Castillo, E., Colosimo, B. M., and Tajbakhsh, S. D. (2015), “Geodesic Gaussian Processes for the Parametric Reconstruction of a Free-Form Surface,” *Technometrics*, 57, 87–99.
- Egozcue, J. J., Díaz-Barrero, J. L., and Pawlowsky-Glahn, V. (2006), “Hilbert Space of Probability Density Functions Based on Aitchison Geometry,” *Acta Mathematica Sinica*, 22, 1175–1182.
- Garg, A., Tai, K., Lee, C. H., and Savalani, M. M. (2014), “A Hybrid M5’-Genetic Programming Approach for Ensuring Greater Trustworthiness of Prediction Ability in Modelling of FDM Process,” *Journal of Intelligent Manufacturing*, 25, 1349–1365.
- Hausdorff, F. (1914), *Grundzüge der Mengenlehre*, Leipzig Viet.
- He, K., Zhang, M., Zuo, L., Alhwiti, T., and Megahed, F. M. (2017), “Enhancing the Monitoring of 3D Scanned Manufactured Parts through Projections and Spatiotemporal Control Charts,” *Journal of Intelligent Manufacturing*, 28, 899–911.
- Hron, K., Menafoglio, A., Templ, M., Hrušová, K., and Filzmoser, P. (2016), “Simplicial Principal Component Analysis for Density Functions in Bayes Spaces,” *Computational Statistics & Data Analysis*, 94, 330–350.
- Huang, D., Du, S., Li, G., Zhao, C., and Deng, Y. (2018), “Detection and Monitoring of Defects on Three-Dimensional Curved Surfaces Based on High-Density Point Cloud Data,” *Precision Engineering*, 53, 79–95.
- Karatzoglou, A., Smola, A., and Hornik, K. (2023), *Kernlab: Kernel-based Machine Learning Lab*.

- Karatzoglou, A., Smola, A., Hornik, K., and Zeileis, A. (2004), “Kernlab - an S4 Package for Kernel Methods in R,” *Journal of Statistical Software*, 11, 1–20.
- Kreyszig, E. (1991), *Differential Geometry*, New York: Dover Publications.
- Leblanc, A. (2010), “A Bias-Reduced Approach to Density Estimation Using Bernstein Polynomials,” *Journal of Nonparametric Statistics*, 22, 459–475.
- Li, X., Xu, G., and Zhang, Y. J. (2015), “Localized Discrete Laplace–Beltrami Operator over Triangular Mesh,” *Computer Aided Geometric Design*, 39, 67–82.
- Mardia, K. V., Kent, J. T., Kent, J. T., and Bibby, J. M. (1979), *Multivariate Analysis*, Academic Press.
- Megahed, F., Wells, L., and Camelio, J. (2010), “The Use of 3D Laser Scanners in Statistical Process Control,” SAE Technical Paper 2010-01-1864, SAE International, Warrendale, PA.
- Menafoglio, A., Grasso, M., Secchi, P., and Colosimo, B. M. (2018), “Profile Monitoring of Probability Density Functions via Simplicial Functional PCA With Application to Image Data,” *Technometrics*, 60, 497–510.
- Montgomery, D. C. (2020), *Introduction to Statistical Quality Control*, Wiley, 8th edition.
- Oja, H. (2010), *Multivariate Nonparametric Methods with R: An Approach Based on Spatial Signs and Ranks*, Lecture Notes in Statistics, New York: Springer-Verlag.
- Patanè, G. (2017), *An Introduction to Laplacian Spectral Distances and Kernels: Theory, Computation, and Applications*, Synthesis Lectures on Visual Computing: Computer Graphics, Animation, Computational Photography and Imaging, Cham: Springer International Publishing.
- Pesarin, F. (2001), *Multivariate Permutation Tests : With Applications in Biostatistics*, Chichester ; New York: Wiley, 1st edition edition.

- Qiu, P. (2013), *Introduction to Statistical Process Control*, Boca Raton: CRC Press.
- Ramsay, J. and Silverman, B. W. (2005), *Functional Data Analysis*, Springer Series in Statistics, New York: Springer-Verlag, 2 edition.
- Ramsay, J. O. and Silverman, B. W. (2002), *Applied Functional Data Analysis: Methods and Case Studies*, Springer Series in Statistics, New York: Springer-Verlag.
- Reuter, M., Wolter, F.-E., Shenton, M., and Niethammer, M. (2009), “Laplace–Beltrami Eigenvalues and Topological Features of Eigenfunctions for Statistical Shape Analysis,” *Computer-Aided Design*, 41, 739–755.
- Schölkopf, B., Smola, A., and Müller, K.-R. (1998), “Nonlinear Component Analysis as a Kernel Eigenvalue Problem,” *Neural Computation*, 10, 1299–1319.
- Scimone, R., Taormina, T., Colosimo, B. M., Grasso, M., Menafoglio, A., and Secchi, P. (2022), “Statistical Modeling and Monitoring of Geometrical Deviations in Complex Shapes With Application to Additive Manufacturing,” *Technometrics*, 64, 437–456.
- Shang, H. L. (2014), “A Survey of Functional Principal Component Analysis,” *AStA Advances in Statistical Analysis*, 98, 121–142.
- Šidák, Z. (1967), “Rectangular Confidence Regions for the Means of Multivariate Normal Distributions,” *Journal of the American Statistical Association*, 62, 626–633.
- Sood, A. K., Chaturvedi, V., Datta, S., and Mahapatra, S. S. (2011), “Optimization of Process Parameters in Fused Deposition Modeling Using Weighted Principal Component Analysis,” *Journal of Advanced Manufacturing Systems*, 10, 241–259.
- Stankus, S. E. and Castillo-Villar, K. K. (2019), “An Improved Multivariate Generalised Likelihood Ratio Control Chart for the Monitoring of Point Clouds from 3D Laser Scanners,” *International Journal of Production Research*, 57, 2344–2355.
- van den Boogaart, K. G., Egozcue, J. J., and Pawlowsky-Glahn, V. (2014), “Bayes Hilbert Spaces,” *Australian & New Zealand Journal of Statistics*, 56, 171–194.

- Vitale, R. A. (1975), “A Bernstein Polynomial Approach to Density Function Estimation,” in Puri, M. L. (editor), *Statistical Inference and Related Topics*, Academic Press, 87–99.
- Wang, A., Wang, K., and Tsung, F. (2014), “Statistical Surface Monitoring by Spatial-Structure Modeling,” *Journal of Quality Technology*, 46, 359–376.
- Wells, L. J., Megahed, F. M., Niziolek, C. B., Camelio, J. A., and Woodall, W. H. (2013), “Statistical Process Monitoring Approach for High-Density Point Clouds,” *Journal of Intelligent Manufacturing*, 24, 1267–1279.
- Woodall, W. H., Spitzner, D. J., Montgomery, D. C., and Gupta, S. (2004), “Using Control Charts to Monitor Process and Product Quality Profiles,” *Journal of Quality Technology*, 36, 309–320.
- Wuest, T., Irgens, C., and Thoben, K.-D. (2014), “An Approach to Monitoring Quality in Manufacturing Using Supervised Machine Learning on Product State Data,” *Journal of Intelligent Manufacturing*, 25, 1167–1180.
- Zang, Y. and Qiu, P. (2018a), “Phase I Monitoring of Spatial Surface Data from 3D Printing,” *Technometrics*, 60, 169–180.
- Zang, Y. and Qiu, P. (2018b), “Phase II Monitoring of Free-Form Surfaces: An Application to 3D Printing,” *Journal of Quality Technology*, 50, 379–390.
- Zhao, C., Lv, J., and Du, S. (2022), “Geometrical Deviation Modeling and Monitoring of 3D Surface Based on Multi-Output Gaussian Process,” *Measurement*, 199, 111569.
- Zhao, X. (2022), *Intrinsic Geometrical Methods for Statistical Process Control of Complex Data Objects*, Ph.D. thesis.
- Zhao, X. and del Castillo, E. (2021), “An Intrinsic Geometrical Approach for Statistical Process Control of Surface and Manifold Data,” *Technometrics*, 63, 295–312.

Zhu, L., Brereton, R. G., Thompson, D. R., Hopkins, P. L., and Escott, R. E. A. (2007), “On-Line HPLC Combined with Multivariate Statistical Process Control for the Monitoring of Reactions,” *Analytica Chimica Acta*, 584, 370–378.

Zou, H. (2006), “The Adaptive Lasso and Its Oracle Properties,” *Journal of the American Statistical Association*, 101, 1418–1429.

A Simplicial Functional Principal Component Analysis (SFPCA)

Simplicial functional principal component analysis (SFPCA) is an extension of functional principal component analysis which can be applied to functions belonging to the Bayes space B^2 ,

$$B^2 = \left\{ f : f > 0, \int_0^t f(t)dt = c, \log(f) \in L^2 \right\}. \quad (\text{A.1})$$

SFPCA identifies the directions $\xi_1, \dots, \xi_{N-1} \in B^2$ that exhibit maximal variability in the observed data. The space B^2 is the infinite-dimensional generalization of the more common Aitchison simplex for compositional data (Aitchison, 2003). This space has been studied and suitable operations including an inner product $\langle \cdot, \cdot \rangle_{B^2}$ and a norm $\| \cdot \|_{B^2}$ have been defined (Egozcue et al., 2006; van den Boogaart et al., 2014) For the data set $\mathbf{f}_S = \{ \hat{f}_{S_j}, j = 1, \dots, N \}$ (see Section 2.1), the first simplicial principal component ξ_1 aims to maximize

$$\sum_{j=1}^N \langle \hat{f}_{S_j} - \bar{f}_S, \xi^{(S)} \rangle_{B^2}^2 \text{ subject to } \|\xi^{(S)}\|_{B^2} = 1, \quad (\text{A.2})$$

\bar{f}_S is the sample mean of \mathbf{f}_S , $j = 1, \dots, N$. For $j > 1$, ξ_j maximizes

$$\sum_{j=1}^N \langle \hat{f}_{S_j} - \bar{f}_S, \xi^{(S)} \rangle_{B^2}^2 \text{ subject to } \|\xi^{(S)}\| = 1, \langle \xi^{(S)}, \xi_i^{(S)} \rangle = 0, \quad \forall i < j. \quad (\text{A.3})$$

After applying SFPCA to \mathbf{f}_S , a sequence of $N - 1$ pairs of eigenvalues and eigenvectors $(\lambda_i^{(S)}, \xi_i^{(S)})$ is obtained. As is customary in standard principal component analysis, the pairs are arranged so that the eigenvalues form a non-increasing sequence and the eigenvectors are orthonormal. It is also possible to obtain the score of \hat{f}_{S_j} , $j = 1, \dots, N$, along the i -th principal component, $i = 1, \dots, N - 1$, as $z_{ji}^{(S)} = \langle \hat{f}_{S_j} - \bar{f}_S, \xi_i^{(S)} \rangle$, which represents the projection of the original PDF j onto the i -th direction. The number of principal components, denoted as $K^{(S)}$, is determined based on the fraction of explained variance. The same procedure is applied to \mathbf{f}_P , resulting in the $K^{(P)}$ principal components $\xi_i^{(P)}$, their eigenvalues $\lambda_i^{(P)}$, and scores $z_{ji}^{(P)}$.

Calculation of the simplicial principal components as defined by Equations (A.2) and (A.3) requires a complicated maximisation procedure, as each solution has to be found within the set of functions belonging to the Bayes space B^2 . However, [Hron et al. \(2016\)](#) show that calculating SFPCA is equivalent to calculating functional principal component analysis ([Ramsay and Silverman, 2002, 2005](#); [Shang, 2014](#), FPCA, see, for example,) on a suitable transformation of the PDFs, called the centered log-ratio transformation (CLR).

Let $f \in B^2$ be a density with support $[a, b]$. The CLR transform of f is defined as:

$$[\text{clr}(f)](t) = \log(f(t)) - \frac{1}{b-a} \int_a^b \log(f(\tau)) d\tau, \quad t \in [a, b]. \quad (\text{A.4})$$

Equation (A.4) allows mapping densities from the space B^2 into the space of twice-integrable real functions, where traditional FPCA can be applied. The clr transformation is calculated from the estimated PDFs and evaluated at a discrete set of points in their support.

A.1 Monitoring Statistics Using SFPCA

Suitable T^2 and Q monitoring statistics for checking the stability of \mathbf{f}_S can be defined as

$$T_j^{2(S)} = \sum_{i=1}^{K^{(S)}} \frac{z_{ji}^{(S)2}}{\lambda_i^{(S)}}, \quad (\text{A.5})$$

and

$$Q_j^{(S)} = \|\hat{f}_{S_j} - f_{S_j}^*\|^2, \quad (\text{A.6})$$

where $f_{S_j}^* = \bar{f}_S + \sum_{i=1}^{K^{(S)}} z_{ji} \xi_i^{(S)}$ is the reconstruction of \hat{f}_{S_j} obtained by considering the first $K^{(S)}$ principal components. The same procedure is followed for \mathbf{f}_P , resulting in the control statistics $(T^{2(P)}, Q^{(P)})$. To determine the control limits of the control statistics, a desired overall FAP of α^* is set and a corrected. Assuming the monitoring statistics for \mathbf{f}_S and \mathbf{f}_P to be correlated, the FAP for each pair of control charts can be calculated using Bonferroni correction (Bonferroni, 1936) as $\alpha' = \alpha^*/2$. Note that, for each pair of monitoring statistics, the T^2 statistic monitors the reconstruction obtained by the SFPCA, whereas the Q statistic monitors changes in the orthogonal component. Therefore, independence between the T^2 and Q statistics may be assumed and the FAP for each of the four control charts is given by $\alpha = 1 - \sqrt{1 - \alpha'}$ (Šidák, 1967). The control limit for the T^2 charts is given by Scimone et al. (2022) as:

$$UCL_\alpha(T^2) = \frac{(N-1)^2}{N} q_{Beta(1-\alpha, K/2, (N-K-1)/2)}, \quad (\text{A.7})$$

where $K = K^{(S)}$ for the T^2 chart related to \mathbf{f}_S , or $K = K^{(P)}$ for the T^2 chart related to \mathbf{f}_P , and $q_{Beta(1-\alpha, a, b)}$ is the $(1 - \alpha)$ quantile of the Beta(a, b) distribution (Montgomery, 2020). The control limit for the Q charts is defined as

$$UCL_\alpha(Q) = \theta_1 \left\{ 1 - \theta_2 h_0 \left(\frac{1 - h_0}{\theta_1^2} \right) + \frac{\sqrt{z_\alpha (2\theta_2 h_0^2)}}{\theta_1} \right\}^{\frac{1}{h_0}}, \quad (\text{A.8})$$

where z_α is the $(1 - \alpha)$ quantile of the normal distribution, $h_0 = 1 - \frac{(2\theta_1\theta_3)}{3\theta_2^2}$, $\theta_r = \sum_{j=K+1}^{\infty} \lambda_j^r$, $r = 1, 2, 3$, and λ_j are the eigenvalues obtained from the SFPCA of \mathbf{f}_S and \mathbf{f}_P (Zhu et al., 2007).

A.2 Differential Geometry

A.2.1 Generalities on Differential Geometry

We now briefly review some elements of differential geometry necessary to introduce the Laplace-Beltrami operator used in the chart proposed by [Zhao and del Castillo \(2021\)](#). For an in-depth introduction to differential geometry, refer to [Kreyszig \(1991\)](#). Let $f : \mathbb{R}^n \rightarrow \mathbb{R}$ be a twice differentiable function, and define its gradient as the vector of partial derivatives of f with respect to the coordinates x_1, \dots, x_n ,

$$\nabla f = \left(\frac{\partial f}{\partial x_1}, \dots, \frac{\partial f}{\partial x_n} \right)^\top. \quad (\text{A.9})$$

The divergence of the vector ∇f is defined as the sum of the partial derivatives of its elements with respect to the coordinates x_1, \dots, x_n ,

$$\text{div } \nabla f = \frac{\partial}{\partial x_1} \left(\frac{\partial f}{\partial x_1} \right) + \dots + \frac{\partial}{\partial x_n} \left(\frac{\partial f}{\partial x_n} \right). \quad (\text{A.10})$$

The Laplace operator or Laplacian of the function f is given by:

$$\Delta f = -\text{div } \nabla f = -\sum_{i=1}^n \frac{\partial^2 f}{\partial x_i^2}. \quad (\text{A.11})$$

The Laplace operator in Equation (A.11) is based on the second partial derivatives of f . Therefore, it is directly related to the curvature of f in the neighborhood of each point of the domain.

A.2.2 Laplace-Beltrami operator

An extension of the Laplacian, which is used in the case where the domain of f is not \mathbb{R}^n but a k -dimensional manifold \mathcal{M} enclosed in an n -dimensional Euclidean space, is given by the Laplace-Beltrami operator. More formally, for a function $f : \mathcal{M} \rightarrow \mathbb{R}$, the Laplace-

Beltrami (LB) operator is defined as:

$$\Delta_{\mathcal{M}}f = -\text{div}_{\mathcal{M}}\nabla_{\mathcal{M}}f. \quad (\text{A.12})$$

Here, $\nabla_{\mathcal{M}}f$ and $\text{div}_{\mathcal{M}}$ are respectively the gradient and divergence computed on the manifold \mathcal{M} . In the case study from Section 3, we monitor the surface of the manufactured objects, which can be considered a 2-dimensional manifold embedded in a 3-dimensional ambient space. Therefore, $\dim \mathcal{M} = 2$, and thus the surface of such a manifold can be described by $\mathbf{p}(x^1, x^2) = (x(x^1, x^2), y(x^1, x^2), z(x^1, x^2))^{\top}$. The coordinates of the manifold are represented with superscripts instead of subscript for coherence with the standard notation of differential geometry (Kreyszig, 1991). Let \mathbf{p}_{x^1} and \mathbf{p}_{x^2} be the vectors of the partial derivatives of the elements of $\mathbf{p}(x^1, x^2)$ with respect to the coordinates x^1 and x^2 . Let

$$G = \begin{pmatrix} g_{11} & g_{12} \\ g_{12} & g_{22} \end{pmatrix},$$

where $g_{ij} = \langle \mathbf{p}_{x^i}, \mathbf{p}_{x^j} \rangle$, for $i, j = 1, 2$. The LB operator of a function $f(x^1, x^2)$ is given by

$$\Delta_{\mathcal{M}}f = -\frac{1}{\sqrt{\det(G)}} \sum_{j=1}^2 \frac{\partial}{\partial x^j} \left(\sqrt{\det(G)} \sum_{i=1}^2 g^{ij} \frac{\partial f}{\partial x^i} \right),$$

where g^{ij} is the (i, j) -th element of G^{-1} . The LB operator is an intrinsic measure of the local curvature of a function, which takes into account the curvature of both the ambient space and the manifold. For manufactured objects, the true function f is unknown and the manifold is reconstructed via point cloud or meshes obtained using noncontact measurement tools. This “discretized” version of the manifold reduces the continuous function f defined on \mathcal{M} to a vector, whose elements correspond to the values of the function f at the observed points. Zhao and del Castillo (2021) therefore use a discrete version of the LB operator originally proposed by Li et al. (2015) for mesh data.

Let \mathcal{M} be a manifold with m observed points p_1, \dots, p_m , and let $f(p_i)$, $i = 1, \dots, m$,

be the values of the function f evaluated at these points. The discrete Laplace-Beltrami operator is a matrix L^t , of size $m \times m$, whose elements are given by the values of the operator calculated at $f(p_i)$, $i = 1, \dots, m$,

$$L^t f(p_i) = \frac{1}{4\pi t^2} \sum_{p_j: d_{geo}(p_i, p_j) \leq r} \frac{A(p_j)}{3} e^{-\frac{d_{geo}(p_i, p_j)^2}{4t}} [f(p_i) - f(p_j)], \quad j = 1, \dots, m, \quad (\text{A.13})$$

Here, d_{geo} represents the geodesic distance between two points, r is a preset value, $A(p_j)$ is the area of the neighborhood of point p_j , and t is a parameter related to the size of the area of interest around p_i . Equation (A.13) only considers points p_j within a radius r of p_i , which reduces memory usage and computational cost as the resulting matrix is sparse.

A.2.3 Computational Aspects of the Laplace-Beltrami Operator

The matrix L^t of size $m \times m$ and containing the discrete LB operator evaluated at points p_i , $i = 1, \dots, m$ is obtained as

$$L^t = D - W. \quad (\text{A.14})$$

Here, $W_{ij} = \frac{1}{12\pi t^2} A(p_j) e^{d_{geo}(p_i, p_j)^2/4t}$ and D is a diagonal matrix with elements $D_{ii} = \sum_j W_{ij}$ (Zhao and del Castillo, 2021). The matrix L^t can be represented as the product of two matrices such that

$$L^t = B^{-1}C, \quad (\text{A.15})$$

where B is a diagonal matrix and C is a positive semidefinite symmetric matrix (Patanè, 2017). The elements on the diagonal of matrix B are given by the areas $A(p_i)$, $i = 1, \dots, m$, of the neighborhoods of each point p_i (Zhao, 2022).

Equation (A.15) implies that L^t is invertible and ensures that the eigenvalues of L^t are real. Moreover, it is shown that $B^{-1}C$ has the same eigenvalues as the symmetric matrix $B^{-1/2}CB^{-1/2}$ (Zhao, 2022). Since $C = BL^t$ from Equation (A.15), finding the eigenvalues

of $B^{-1}C$ is equivalent to calculating the eigenvalues of the symmetric matrix

$$L_{sym} = B^{1/2}L^tB^{-1/2}. \tag{A.16}$$

Therefore, it is possible to perform the spectral decomposition of Equation (A.16) instead of Equation (A.15). This allows the exploitation of the computational advantages resulting from the symmetry of L_{sym} when obtaining the eigenvalues of matrix L^t (Zhao, 2022).